TU Delft

Delft University of Technology

Document Version
Final published version

Licence
CC BY

Citation (APA)
Ragni, D., Arcondoulis, E. J. G., & Fiscaletti, D. (2026). Measurement of dynamic permeability in grazing flows for porous trailing edges. *Flow*, *6*, Article E16. https://doi.org/10.1017/flo.2026.10053

Important note
To cite this publication, please use the final published version (if applicable).
Please check the document version above.

Copyright
In case the licence states “Dutch Copyright Act (Article 25fa)”, this publication was made available Green Open Access via the TU Delft Institutional Repository pursuant to Dutch Copyright Act (Article 25fa, the Taverne amendment). This provision does not affect copyright ownership.
Unless copyright is transferred by contract or statute, it remains with the copyright holder.

Sharing and reuse
Other than for strictly personal use, it is not permitted to download, forward or distribute the text or part of it, without the consent of the author(s) and/or copyright holder(s), unless the work is under an open content license such as Creative Commons.

Takedown policy
Please contact us and provide details if you believe this document breaches copyrights.
We will remove access to the work immediately and investigate your claim.

This work is downloaded from Delft University of Technology.

Flow (2026), **6** E16
doi:10.1017/flo.2026.10053

FLOW CAMBRIDGE UNIVERSITY PRESS

RESEARCH ARTICLE

Measurement of dynamic permeability in grazing flows for porous trailing edges

Daniele Ragni[1], Elias J. G. Arcondoulis[2] and Daniele Fiscaletti[3]

[1]Faculty of Aerospace, Delft University of Technology, 2629 HS Delft, Netherlands
[2]Institute of Sound and Vibration Research, University of Southampton, Southampton SO17 1BJ, UK
[3]Faculty of Mechanical Engineering, Delft University of Technology, 2628 CD Delft, Netherlands
Corresponding author: Daniele Ragni; Email: d.ragni@tudelft.nl

Received: 18 August 2025 UTC; **Revised:** 27 March 2026 UTC; **Accepted:** 26 April 2026 UTC

Keywords: blunt trailing edge; dynamic permeability; porous materials

Abstract

Porous trailing edges attenuate hydrodynamic pressure fluctuations that scatter as trailing-edge noise, with their effectiveness governed by their material parameters. Conventional measurements of permeability rely on steady-flow rigs, which cannot capture the dynamic response of this parameter, which is relevant for predicting balancing pressure fluctuations under grazing-flow conditions. In this study, we introduce a method for directly determining the dynamic permeability of porous trailing edges from time-resolved particle image velocimetry (PIV) data. The approach employs a lumped-system circuit analogy that links unsteady pressure gradients to through-material velocities, enabling *in situ* characterisation without specialised porous rigs, thereby further extending its applicability to thin trailing-edge geometries. Two materials with similar porosity but distinct internal architectures are compared against a solid baseline: a structured porous trailing edge (SPTE) and a random foam trailing edge (RFTE). The extracted permeability curves show close agreement with the analytical model of Johnson *et al*. (*J. Fluid Mech.*, 1987, vol. 176, pp. 379–402), validating the method for both structured and randomised porous materials. The procedure also allows for the estimation of the equivalent viscous characteristic length and tortuosity. A detailed comparison reveals that the SPTE exhibits a lower viscous length scale and tortuosity than the RFTE, with a relatively higher dynamic permeability response at high frequencies.

Impact Statement

Porous trailing edges are widely used to mitigate turbulent boundary-layer fluctuations and the associated scattering of trailing-edge noise. Their performance is governed by porosity and permeability, yet these properties are typically determined only in dedicated steady-flow rigs that cannot easily reproduce unsteady hydrodynamic pressure fluctuations. We demonstrate a new method for measuring the dynamic permeability of porous materials directly under grazing-flow conditions, utilising time-resolved PIV and a lumped-system circuit analogy. This approach reveals how unsteady pressure gradients couple with through-material velocities, enabling permeability characterisation for thin trailing edges where traditional rigs are impractical. In particular, we find that internal architecture strongly governs the frequency-dependent permeability response. This work enables the study of porous add-on architectures with laser velocimetry, simplifying the design of permeable materials with targeted aerodynamic and acoustic performance.

© The Author(s), 2026. Published by Cambridge University Press. This is an Open Access article, distributed under the terms of the Creative Commons Attribution licence (https://creativecommons.org/licenses/by/4.0/), which permits unrestricted re-use, distribution and reproduction, provided the original article is properly cited.

https://doi.org/10.1017/flo.2026.10053 Published online by Cambridge University Press

1. Introduction

The scattering of pressure fluctuations from a turbulent boundary layer at an airfoil trailing edge in uniform, homogeneous flow is a significant contributor to broadband self-noise (Brooks *et al*. 1989). According to Blake (2012), when the trailing-edge thickness, t, of an airfoil is greater than approximately four times the displacement thickness, δ^*, of the incoming turbulent boundary layers from both sides, the unsteady lift fluctuations determined by the Karman vortex shedding instability scatter in the form of a unique tonal noise contribution, in an otherwise broadband acoustic emission. The most significant tonal harmonic frequency, f, can be computed by assuming a Strouhal number of $St = ft/V_\infty \approx 0.2$, where V_∞ is the free-stream velocity. Such acoustic emissions are usually referred to as blunt trailing-edge noise, and are characterised by a narrow-band component, dependent on the energy cascade of the flow-pressure fluctuations at the trailing edge. The tonal component of the acoustic spectrum is a byproduct of the scattering of pressure fluctuations due to vortex shedding associated with the roll-up process in the near wake. Therefore, efforts to mitigate this noise have focused on suppressing vortical fluctuations generated by the trailing edge.

1.1. Permeability and noise reduction by porous materials

The genesis and evolution of flow instabilities in the wake of bluff bodies have been widely studied for both aerodynamic and aeroacoustic purposes (Barbi *et al*. 1986; Lee & Budwig 1991). To reduce unsteady-flow fluctuations, the most promising flow-control strategies focus on inhibiting coherent vortex shedding by adding turbulent-mixing elements, such as distributed roughness (Achenbach 1971; Kiu *et al*. 2011) or splitter plates (Bearman 1965; Kwon & Choi 1996). The physical mechanisms behind such flow-control strategies have been found to rely upon two effects: the elongation of the streamwise length scales of the vortical flow structures, allowing the pressure difference of the boundary layers on both sides of the model to reduce before the roll-up; and the promotion of turbulent fluctuations enhancing flow entrainment and anticipated mixing of the coherent vortices deploying from the body. However, a significant challenge lies in implementing a flow-control strategy that minimises drag. Inspired by the velvety characteristics of owls' wings (Graham 1934; Jaworski and Peake 2020), the application of porous materials at the edge of an airfoil revealed pressure fluctuation mitigation and noise reduction relative to a solid baseline (Geyer *et al*. 2010*a*, *b*). Although measurements using trailing-edge inserts confirmed that the noise reduction is proportional to the permeability of the porous medium (Ali *et al*. 2018; Rubio-Carpio *et al*. 2019), the drag estimation was found to be proportional to the length of the insert.

Although the permeability of the porous medium is derived from fitting pressure losses to flow velocity at the exit of porous materials in permeability rigs, a study by Teruna *et al*. (2021) shows that this approach may yield inaccurate permeability predictions when the material thickness is very thin, particularly for trailing-edge noise applications. In particular, the material thickness may initially be proportional to multiple pore sizes and taper linearly to zero, thereby complicating accurate assessment of flow response to permeability. Teruna *et al*. (2021) also revealed that a region of intense velocity and pressure fluctuations within the porous medium is present, which the authors characterised by defining an 'entrance length'. Although the authors reported that the pressure-release mechanism was present when the material thickness was proportional to a multiple of the entrance length, the study did not explain why or how this conclusion could be applied to evaluate the actual flow response to the particular material choice. It remains unexplained how the development of the boundary layer affected the pressure gradient along and across the porous insert, as well as the role of the decreasing trailing-edge thickness.

Porous materials were also applied to suppress vortical shedding in the wake of a porous cylinder, to abate the well-known aeolian tones expected in the far-field acoustic pressure (Sueki *et al*. 2010). Numerical simulations of Naito and Fukagata (2012) confirmed that the flow communication imposed by the material porosity promoted the attenuation of the pressure and lift fluctuations at the onset of the shear layers, largely due to the greater dissipation of turbulent kinetic energy within the porous medium and the non-zero slip velocity on the surface. Since the first publications on noise reduction in cylinders in uniform flow, the adoption of porous materials for passive flow and noise control has grown rapidly. Geyer (2020) conducted comprehensive experimental campaigns to assess the behaviour of various

https://doi.org/10.1017/flo.2026.10053 Published online by Cambridge University Press

porous materials with different airflow resistivities. The porous materials were not observed to lead to a complete suppression of the vortex shedding tone, as found by Klausmann and Ruck (2017) among others, but to a considerable narrowing of the tonal peak. Furthermore, the peak shifted towards lower Strouhal numbers for porous materials with relatively high permeability and towards higher Strouhal numbers for porous materials with relatively low permeability. The Strouhal number shift was also measured and explained by Arcondoulis *et al*. (2023) as the ratio of the peak shear-layer velocity of a porous-coated cylinder to that of an untreated cylinder.

1.2. Frequency response of dynamic permeability

The frequency response of a porous material subject to turbulent flow is a relevant problem across a wide range of disciplines and shows strong Reynolds-number dependence. Wood *et al*. (2020) discuss the frequency response variance with Reynolds number across packed-bed catalysis studies to near-surface atmospheric flows over urban environments. More in detail, the response of a fluid entrained in a rigid porous medium to harmonic pressure fluctuations has been studied across a wide range of problems, including pressure-diffusion analysis (Chandler 1981) and acoustic absorption (Lafarge *et al*. 1997). The description of unsteady incompressible single-phase flow in porous media has long relied on extensions of the steady version of Darcy's law (Lasseux *et al*. 2019). Most studies rely on the dynamic permeability $k(\omega)$ to model macroscopic flow through porous materials under unsteady conditions (Cortis *et al*. 2003). Sheng and Zhou (1988) proposed to scale the predicted dynamic permeability, $k(\omega)$, by the static permeability, k_0, in order to produce a universal transfer function when plotted against a conveniently chosen scaling frequency (ω_c), dependent on the porous material's internal structure and its corresponding properties

$$\frac{k(\omega)}{k_0} = f\left(\frac{\omega}{\omega_c}\right). \tag{1.1}$$

The assumptions behind these studies are that an unsteady pressure drop is imposed at the two ends of a rig where a material specimen is installed. Provided that the characteristic length of the material is orders of magnitude larger than the inner material pore size, analytical models for the oscillatory motion of the flow through the porous material are available. The model originally developed by Johnson *et al*. (1987), for example, is derived analytically utilising the normalised frequency-dependent permeability as the main parameter to describe the flow response to the pressure gradient

$$\frac{k_0}{k(\omega)} = \left(1 - \frac{4i\alpha_\infty^2 k_0^2 \rho_f \omega}{\mu \Lambda^2 \phi^2}\right)^{\frac{1}{2}} - \frac{i\alpha_\infty k_0 \rho_f \omega}{\mu \phi}. \tag{1.2}$$

In (1.2), k_0 is the real-valued permeability conventionally measured in an experiment in which the sample is subjected to a static pressure drop, ϕ is the pore volume fraction, ρ_f is the fluid density and Λ is the viscous length scale of the equivalent fluid channel associated with the material. The term α_∞ is the tortuosity, which corresponds to the apparent mass density enlargement factor that the fluid experiences moving through a porous solid, and the inclusion of the ∞ subscript indicates that boundary-layer effects within the pore volume are neglected. While this model yields a good approximation for several applications (Charlaix *et al*. 1988; Sheng & Zhou 1988), deriving these parameters for materials with a complex internal structure and variable thickness requires evaluating the permeability coefficient in different directions and over a wide range of pressure gradients, which is not always feasible. An alternative approach is to measure the dynamic permeability from unsteady measurements on a permeability test rig; however, this requires the implementation of high-accuracy unsteady pressure gradients in air, which is extremely difficult and impractical.

1.3. Contribution and outline

The present study introduces a new experimental framework for measuring the dynamic permeability of porous trailing edges under grazing flow, eliminating the need for dedicated steady-flow permeability

https://doi.org/10.1017/flo.2026.10053 Published online by Cambridge University Press

rigs. The method is based on time-resolved particle image velocimetry (PIV) measurements and a lumped-system circuit analogy that links unsteady pressure gradients to through-material velocity in regions of strong flow communication. This enables the measurement of the frequency response of permeability, particularly for thin trailing-edge geometries where conventional methods are impractical. To demonstrate the approach, we compare two porous trailing edges with similar porosity but distinct internal architectures: a structured porous trailing edge (SPTE) already studied by Arcondoulis *et al*., (2025, 2024) and Liu *et al*. (2023), and a randomised foam trailing edge (RFTE), with isotropic pore distribution and comparable porosity but different internal architecture (Arcondoulis *et al*. 2025, 2024). Both are tested alongside a solid trailing-edge baseline. We demonstrate that the proposed method reproduces the analytical trends of Johnson *et al*. (1987) while revealing architecture-dependent differences in permeability decay rates and coherent flow communication bandwidths. The paper is organised as follows: Section 2 introduces the experimental model and measurement techniques. Section 3 presents statistical results for all trailing edges. Section 4 outlines the proposed methodology and unsteady material response. Finally, Section 5 summarises the main findings and implications for aeroacoustic applications.

2. Experimental apparatus

2.1. Water flume model and porous inserts

An elliptical leading-edge flat plate with a length of 350 mm, a height of 25 mm and a width of 400 mm was installed in the low-speed water flume of the Department of Civil Engineering and Geosciences at TU Delft, as part of an experimental regime where preliminary results are presented in Arcondoulis *et al*. (2025). The flume is effectively a channel confined on the bottom and on the sides, but open in the direction of the flow and at the top of the model for access to the sample. The flume has a test section of 400 mm width and 300 mm height. Control of the free-stream velocity is provided by a system featuring a centrifugal pump and a valve, enabling operation at a maximum speed of $1.2\ \mathrm{m\ s^{-1}}$. A free-stream velocity of $V_\infty = 0.15\ \mathrm{m\ s^{-1}}$ was used in this study. The water temperature was measured to be at $18\ ^\circ\mathrm{C}$, to give a kinematic viscosity of $\nu = 1.053 \times 10^{-6}\ \mathrm{m^2 s^{-1}}$ and a density $\rho = 998.6\ \mathrm{kg\ m^{-3}}$. These properties are used for the data processing in the remainder of the manuscript. The flume equivalent inclination is approximately 1° downward for this study, which determines a negligible perturbation of the water surface during the measurement. A schematic diagram of the model is shown in figure 1.

Two different porous materials were appended to the trailing edge of the plate, being a SPTE with a void-fraction porosity of 87 %, and a polyurethane RFTE with a comparable permeability, and a uniform and homogeneous structure with a pore mean diameter of approximately 2 mm. The SPTE, similar to the structured porous-coated cylinder from Arcondoulis *et al*. (2019), has clear lines of sight in the spanwise and vertical directions, and can be customised for a specific porosity and number of pores per inch that are otherwise difficult to achieve with randomised structured porous media. In this study, the SPTE possessed the following internal parameters: $c_1 = 1.88$ mm, $c_2 = 5.00$ mm, $c_3 = 2.5$ mm and $c_4 = 0.74$ mm (see figure 1b). The SPTE was 3D-printed using a transparent ultraviolet-curing epoxy resin to avoid interference with the PIV illumination. Due to 3D-printing limitations, the overall SPTE was joined using three pieces, attached along the spanwise axis, giving the total dimensions of $35 \times 25 \times 400$ mm. A summary of the properties of the materials is presented in Table 1.

The model was placed approximately at $x = 6$ m downstream of the flume entrance. As in Arcondoulis *et al*. (2023), the investigators verified that the water tunnel measurements were not affected by the limited depth of the flume and by the boundary layer developing on its bottom. Estimated with a laminar Blasius profile $\delta(x) = 5\sqrt{x\nu/V_\infty}$ and later verified experimentally, the boundary-layer height was approximately 14 mm, as in Arcondoulis *et al*. (2023). The model was additionally located in the middle of the test section, as shown in figures 1a and 1c. The turbulence intensity of the flow at the streamwise location of the model, i.e. $\sigma_u = u'/V_\infty$, was measured to be approximately 2 %. In the present configuration, the combination of the flume-inclination angle, the low height of the flat plate and the low incoming turbulence allowed neglecting all air–water interface effects, which did not affect laser illumination.

https://doi.org/10.1017/flo.2026.10053 Published online by Cambridge University Press

Table 1. *Summary of the material properties employed for the study. The properties are those needed for the model of Johnson et al. (1987). *The RFTE and SPTE pore diameters are, respectively, from the manufacturer and averaged across the different dimensions*

Acronym	Type of trailing-edge insert	ϕ	Average d [mm]	k_0 [m^2]
STE	Solid baseline trailing edge	0	0	0
SPTE	Structured porous trailing edge	0.87	3.87*	$7{\cdot}10^{-9}$
RFTE	Randomised foam trailing edge	0.80	2.08*	$7{\cdot}10^{-9}$

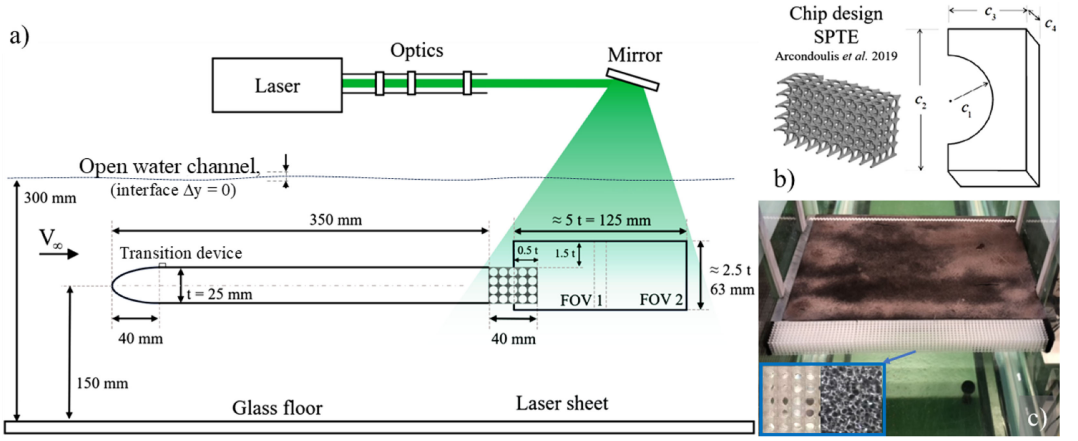


Figure 1. *(a) Schematic diagram of the experimental apparatus and model configuration; (b) chip design of the SPTE; (c) photo of the set-up from above and details of the two permeable trailing edges.*

2.2. Particle image velocimetry set-up, super-sampling and pressure reconstruction

Planar PIV was employed for flow-field measurements, and a schematic of the field of view (FOV) is shown in figure 1a. Fine silicon dioxide particles with a median diameter of 100 μm were used as water seeding, further illuminated by a Quantel EverGreen200 Double-Pulse Nd:YAG laser (532 nm wavelength, 200 mJ per pulse). Laser optics conveyed the illumination to form a laser sheet of approximately 150 $\times$ 1.5 mm. A mirror was used to reflect the laser sheet into the water, as shown in figure 1. Two LaVision sCMOS (16 bit, 4 Mpx resolution, 6.5 μm pixel-pitch) were equipped with 105 μm Nikon Micro-Nikkor lenses to image a FOV of approximately 5 $\times$ 12 cm. Cameras, laser synchronisation and image acquisition were performed using a LaVision programmable timing unit with the LaVision DaVis 10.1 software package. Two sets of 400 images were acquired at 10 Hz, corresponding to approximately ten times the expected vortex shedding frequency of the SPTE of $f \approx 1.2$ Hz (i.e. with a Strouhal number of $St \approx 0.2$ (Arcondoulis *et al*. 2025)). A multi-pass cross-correlation procedure was adopted (Scarano & Riethmuller 1999), with a final interrogation window of 16 $\times$ 16 px and 75 % overlap, ensuring an average concentration of 4 particles per window, appropriate seeding concentration according to Raffel *et al*. (2018). Table 2 summarises the key measurement parameters. The FOV was calibrated with the model in quiescent water using a LaVision Type-7 calibration plate placed in the middle of the laser sheet, resulting in a calibration uncertainty of less than 0.1 px = 2 μm.

Flow statistics in Section 3.1 were obtained by averaging both fields combined over the original maximum number of samples per trailing edge, corresponding to $2N$. However, with a convective velocity proportional to the free stream of 0.15 m s^{-1}, the most energetic flow structures approximately shift by 1 cm between each image pair, corresponding to approximately 1/10$^{\text{th}}$ of the combined FOV. An advection-based model was employed to enhance the time resolution of the flow by super-sampling the vector-field dataset by a factor of 10, following the method described in Scarano and Moore (2012).

https://doi.org/10.1017/flo.2026.10053 Published online by Cambridge University Press

Table 2. *Summary of the experimental parameters*

Free – streamflow V_∞	$0.15\ \mathrm{ms}^{-1}$
Reynolds (V_∞) based on sample t	$Re_t = 3.5 \times 10^3$
Cameras, resolution, pixel pitch	$2 \times$ sCMOS, 2160×2560 px, 6.5×6.5 μm
Imaging focal length, diaphragm	$f = 105$ mm, $f\# = 11$
FOV (i.e. combined 2 cameras)	6.3×12.5 cm
Spatial resolution	16×16 px, 0.37×0.37 mm
Vector spacing (i.e. 75 % overlap)	4×4 px, 0.095×0.095 mm
Acquisition method	Single-frame continuous acquisition
Acquisition frequency f_{aq}	10 Hz
Super-sampling acquisition frequency f_{ss}	100 Hz
Number of datasets per trailing edge	2
Number of samples per dataset N	400
Super-sampled series length N_{ss}	4000

Using two datasets per trailing edge with super-sampling at a frequency of 1.2 Hz, we can ensure spectra are built with a cumulative total of more than 60 cycles at the shedding frequency and more than 150 cycles in the Strouhal number range of interest. The resulting time series are used as an input to compute the velocity material derivative and the pressure gradient. The contributions of the viscous stresses, despite being negligible in this work, close to the trailing edge are included in the material derivative formulation. The pressure reconstruction methodology is derived from previous studies by the authors, based on the material derivative of the flow velocity (Ragni *et al*. 2019). For the interested reader, in this study, the pressure gradient formulation is implemented in Lagrangian form, and the material derivative of the velocity is estimated by least-squares fitting of the velocities along a reconstructed particle trajectory. Two main changes are introduced with respect to the formulation from Pröbsting et al. (2013): the time stencil used to evaluate the material derivative employed a total of 5 vector fields (i.e. reference ± 2 or $n = 2$), and a polynomial of order $m = 2$ is chosen (i.e. a second-order approximation of the flow curvature) for the Lagrangian fit of the vector fields to compute the material derivative. The previous choices were verified to give converged results for the time spectra. The pressure is integrated by setting up a Poisson problem, and by solving the linear system of equations obtained by a second-order accurate central-difference scheme in a preconditioned iterative method (with a 5-point stencil, which was found to be optimal for similar problems, see: Charonko *et al*. (2010), Ragni *et al*. (2009) and van Oudheusden (2013)). Boundary conditions are imposed on the normal components of the pressure gradient. In particular, Neumann boundary conditions are applied along the entire domain except at the top of the boundary layer, where a Dirichlet boundary condition is applied. The latter is obtained by imposing Bernoulli's equation, using the ambient pressure and the free-stream velocity. The Dirichlet condition is set to the wall-normal location of 0.2δ in a manner similar to that of Ghaemi *et al*. (2012), which showed a negligible effect on the calculated wall pressure and a more accurate representation of the relatively larger velocity fluctuations.

2.3. Uncertainty on velocity and pressure fluctuations

For the analysis, we start with the main sources of uncertainty in the velocity computed from this set-up: peak locking, finite spatial resolution and cross-correlation sampling uncertainties. Errors due to peak locking are negligible due to the relatively larger particle size employed. With a digital resolution of $32.7\ \mathrm{px\ mm}^{-1}$, a magnification factor of 0.22 and a diaphragm aperture of 11, the imaged particle on the sensor is approximately 17.4 μm (Adrian & Yao 1985), corresponding to approximately 2.5 px on the sensor. This eliminates peak-locking effects, as was also *a posteriori* verified by plotting the histogram of the round-off values of the particle vector displacements. Errors due to modulation by finite

https://doi.org/10.1017/flo.2026.10053 Published online by Cambridge University Press

spatial resolution are indirectly estimated by assuming that a multi-pass cross-correlation algorithm featuring window deformation requires the length scales of flow structures to be modulated by less than 5 % to be larger than 1.7 times the window size (Schrijer & Scarano 2008). By using a window size of 0.37×0.37 mm, flow structures as small as 0.6 mm can be measured with a 95 % accuracy. Random errors are mainly due to the cross-correlation algorithm. Considering that for the uncertainty the number of samples used for averaging of the single combined fields is 400 at 10 Hz, random errors on the mean velocity fields are $\epsilon_{u,rand} = \sigma_u / \sqrt{N} \approx 0.54\ \mathrm{mm\ s^{-1}}$. Similarly, the uncertainty in the streamwise velocity fluctuations is $\epsilon_{u',rand} = \sigma_u / \sqrt{2(N-1)} \approx 0.39\ \mathrm{mm\ s^{-1}}$. The uncertainty analysis for the reconstructed pressure builds upon the work of Ghaemi *et al*. (2012), Violato *et al*. (2011) and de Kat and van Oudheusden (2012). It begins by evaluating the systematic error, primarily caused by the acceleration between the velocity fields. For the formulation, we refer to the formula as in Boillot and Prasad (1996) corrected by a factor $1/2$ to consider the effect of symmetric window deformation as in Ghaemi *et al*. (2012)

$$\epsilon_{u,sys} = \frac{1}{4} S \Delta t^2 \left| \frac{D\boldsymbol{v}}{Dt} \right|, \tag{2.1}$$

where S is the digital resolution of the system 32.7 px mm^{-1} and $|D\boldsymbol{v}/Dt|$ is the Lagrangian acceleration magnitude obtained by processing multiple vector fields with a time separation Δt. In the present study, adopting the original Δt pertaining to the original time series at 10 Hz would be too conservative and inconsistent with the computation of the material derivative. According to the study by Scarano and Moore (2012), a super-sampling factor of approximately 10 yields a 2 % increase in velocity error. An additional noise averaging process in frequency is introduced, resulting in a fivefold increase in time resolution. Although this does not affect data at lower frequencies, it was established at a much lower resolution and dynamic velocity range because a high-speed system was used in the study. Therefore, assuming the Δt value associated with a super-sampled 100 Hz frequency for the uncertainty evaluation and considering a 2 % increase on the value, with a measured acceleration magnitude below 200 mm s^{-2} in the shear layer, the systematic error in the velocity fields is estimated to be approximately 5 μm corresponding to 0.16 px. Assuming that the Poisson integration does not add significant error to the pressure evaluation, we follow the procedure of Ghaemi *et al*. (2012) by computing the root-mean-square (r.m.s.) of the pressure error from the Navier–Stokes equation, neglecting the viscous term as

$$\epsilon_p \approx \rho\, ds\, \epsilon_{L,rand} = \rho\, ds\, (\epsilon_{L,trunc} + \epsilon_{L,vel}) = \rho\, ds \left(\frac{1}{2} S (n\Delta t)^2 \left| \frac{D\boldsymbol{v}}{Dt} \right| \frac{|\nabla \cdot \boldsymbol{v}|}{\Delta t} + \frac{\epsilon_{u,rand}}{2n\Delta t} \right), \tag{2.2}$$

where ds is the PIV vector resolution. The estimate from the previous equation contains errors due to truncation of the material derivative in the Lagrangian tracking and to random errors in the velocity field. In the present work, the Lagrangian derivative truncation error is higher in the fluctuating shear-layer region. The circle of uncertainty in locating the fluid element at the next time step is, for this study, $c_r = \frac{1}{2} S (n\Delta t)^2 = 1.3$ px or equivalently 0.04 mm. With a typical conservative value of 5 s^{-1} for the divergence in the field and a random velocity error assumed as above to be 0.1 px, the overall error due to truncation and random components for the pressure is 0.08 Pa (to be noted, assuming the density of the water as above 998.6 kg m^{-3} and $n = 2$). However, the use of a planar PIV set-up for flow-pressure reconstruction requires further discussion of the effect of three-dimensional (3-D) flow. Although the paper's methodology for retrieving the dynamic permeability response is based on measurements taken in proximity to the object, the reader should consider that the presence of out-of-plane velocity gradients in its wake creates an additional source of error. Following the work of McClure and Yarusevych (2017), the main indicator for assessing the importance of errors due to 3-D effects is again the divergence of the velocity field. If the flow is well represented by the 2-D gradients, then the velocity field's divergence should be zero, or, equivalently, the residual values should be small relative to the reference gradient across the sample. In figure 2, we have employed the same approach and computed the statistical contribution of the divergence normalised by the characteristic gradient in the flow. The super-sampling procedure operates on planar 2-D velocity fields and does not introduce additional 3-D effects beyond

https://doi.org/10.1017/flo.2026.10053 Published online by Cambridge University Press

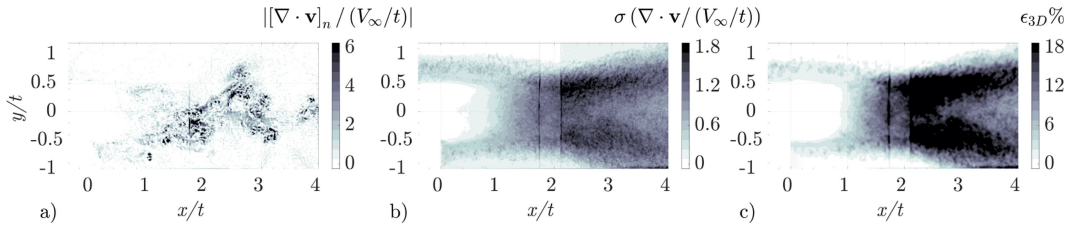


Figure 2. *(a) Instantaneous normalised divergence field for the baseline configuration; (b) standard deviation of the divergence field as computed from the turbulent statistics; (c) percentage error on pressure according to the fit from McClure and Yarusevych (2017).*

those already present in the measured data; equivalently, the 3-D influence on super-sampling is not a major concern for this study. According to the study by McClure and Yarusevych (2017), an error of up to approximately 20 % in pressure due to 3-D flow can be expected in the far part of the wake compared with the 2-D value based on their fit, while in the region where the pressure is extracted for the dynamic permeability, 3-D effects are less important and the error is approximately 5 % of the dynamic pressure.

3. Turbulent wake analysis

3.1. Flow statistics

The mean wake flow statistics of the solid trailing edge (STE), SPTE and RFTE are plotted in figure 3. In this manuscript, we focus purely on the communication effects of the permeable materials. Therefore, more information on the specific aerodynamic performance in terms of momentum-deficit reduction will be omitted, and for the interested reader, it can be found in another study by the same authors (Arcondoulis *et al*. 2025). The turbulent statistics are obtained by averaging the original 2 datasets, each containing 400 images. This also applies to the pressure field, which, after processing for the super-sampled dataset, is downsampled again to the original two 400-image series, for consistency. The convergence of the down-sampled series is verified by monitoring the standard deviation as a function of the number of acquired samples, which is omitted for brevity. The STE in figure 3a–c shows a symmetrical distribution of the streamwise velocity component, as determined by a region of momentum deficit extending to approximately $x/t \approx 2$. After this location, the momentum deficit begins to recover. The wakes behind the SPTE and the RFTE exhibit a shorter momentum deficit, as can be seen by comparing figure 3d–f with figure 3g–i. Compared with the STE, the momentum deficit develops over a shorter downstream distance (to $x/t \approx 1.5$). The mean vertical-velocity component confirms the previous observation. Two regions characterised by approximately 10 %-magnitude vertical-velocity components with opposite signs can be identified at approximately $x/t = [1.2, 0.9, 0.8]$ for the STE, SPTE and RFTE, respectively, indicating a shorter shedding length for the permeable materials and consequently a faster momentum-deficit recovery. The pressure contours in figures 3c, 3f and 3i follow the averaged velocity components. The contours are normalised by the free-stream pressure p_∞ and by the dynamic pressure $1/2\rho V_\infty^2$. The pressure coefficient contours show that the pressure recovers at the maximum extension of the momentum-deficit region. Since the pressure coefficient is found to recover to zero in the FOV for all configurations, it can be concluded that the wake entrainment is fully captured. To verify that the faster recovery of the two porous trailing edges is due to the alteration of the vortex shedding coherence due to permeability, the following section is dedicated to the analysis of the spatio-temporal characteristics of the vortex shedding.

Figure 4 presents the r.m.s. of the fluctuations of the streamwise velocity, vertical velocity and pressure coefficient, for the STE in figure 4a–c, SPTE in figure 4d–f and RFTE in figure 4g–i. The results align with previous studies focusing on permeable materials for the attenuation of Karman vortex instabilities (e.g. Maryami *et al*. (2023)), also identifying the location of the beginning of the flow

https://doi.org/10.1017/flo.2026.10053 Published online by Cambridge University Press

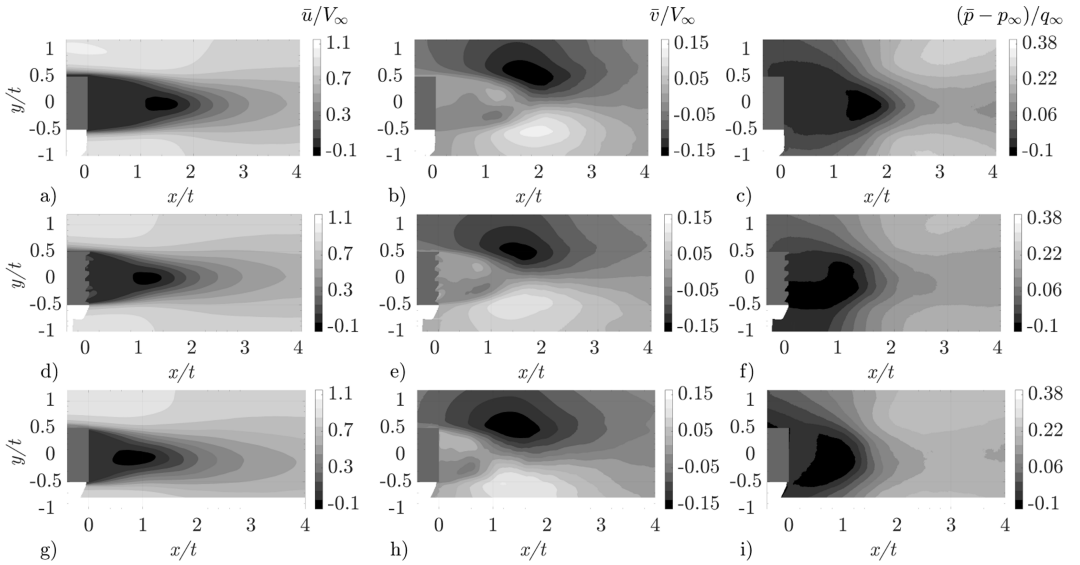


Figure 3. *Normalised time-averaged velocity components, $\overline{u}/V_\infty$ and $\overline{v}/V_\infty$, and normalised time-averaged pressure field, $(\overline{p}-p_\infty)/q_\infty$ for the STE (a–c), structured porous trailing edge SPTE (d–f) and randomised foam trailing edge RFTE (g–i). Flow is from left to right.*

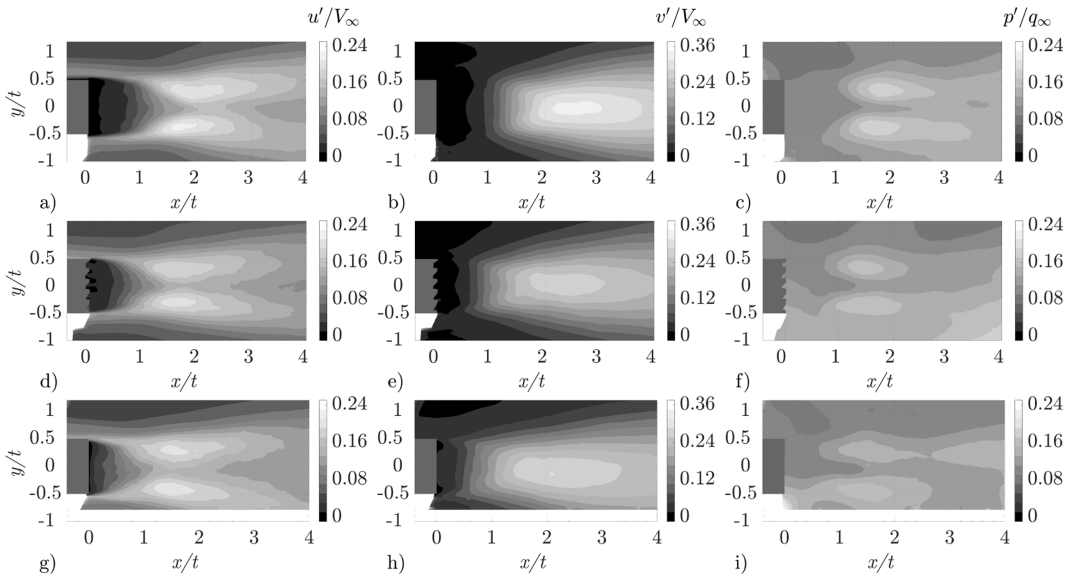


Figure 4. *Normalised r.m.s. of velocity components, u'/V_∞, v'/V_∞ and pressure fluctuations, p'/q_∞, for the STE (a–c), SPTE (d–f) and RFTE (g–i). Flow is from left to right, and q_∞ is calculated as $1/2\rho V_\infty^2$.*

entrainment in the wake with the location where the maximum standard deviation of the velocity components is recorded (Roshko 1954). Figure 4 further illustrates the enhanced attenuation of vortex shedding achieved by the porous materials compared with the STE. In particular, both SPTE and RFTE present lower r.m.s. values than STE across all velocity components, and the location of the respective maximum fluctuations is closer to the trailing-edge location for both porous materials. The contours from the STE, in the top panels of figure 4, show that the maximum fluctuation values are localised at approximately $x/t \lessapprox 2$, consistent with the location at which the wake recovery starts, analogous to the profile

https://doi.org/10.1017/flo.2026.10053 Published online by Cambridge University Press

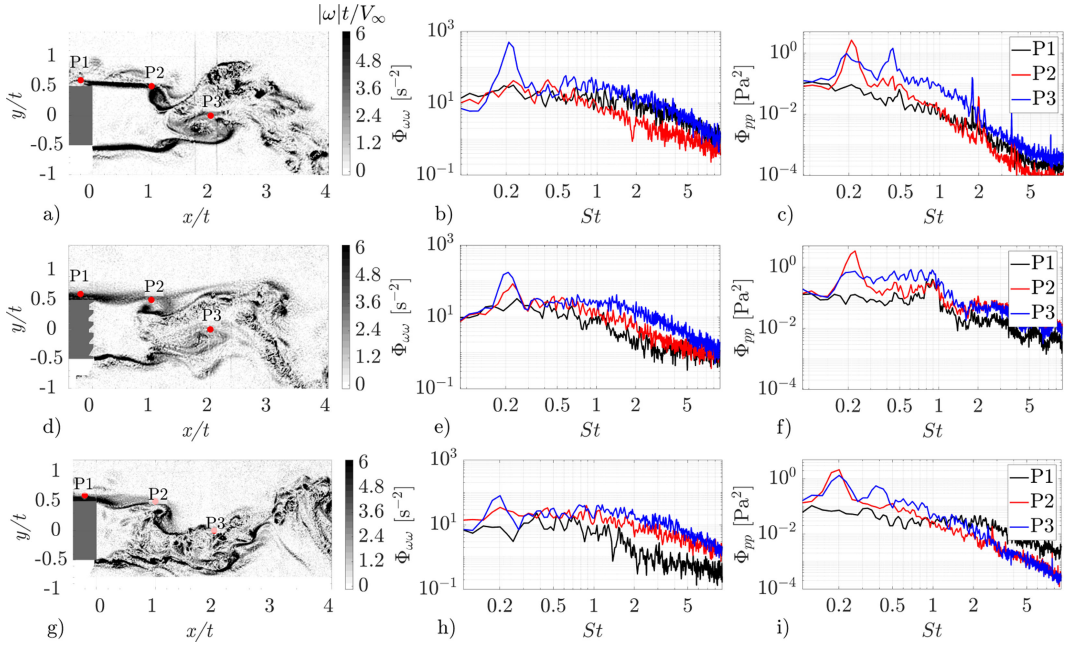


Figure 5. *Left column: maps of normalised instantaneous vorticity, $|\omega|t/V_\infty$, and the positions of three points (P1, P2 and P3) at which auto-spectra are calculated for the (a) STE, (d) SPTE and (g) RFTE. Flow is from left to right. Middle and right columns: auto-spectra of vorticity, $\Phi_{\omega\omega}$ and pressure fluctuations, Φ_{pp}, calculated at P1, P2, P3, for (b, c) the STE, (e, f) the SPTE and (h, i) the RFTE. Note the uncertainty in the velocity and pressure field varying in the FOV in paragraph 2.3.*

distribution from previous studies by Nakamura (1996) and Okajima (1982). By comparing the different materials with respect to the straight trailing edge, an approximately 10 % reduction is observed for the SPTE and RFTE compared with the STE. As also analysed in a study by the same authors (Arcondoulis *et al*. 2025), the rearrangement of the Reynolds stresses in the wake is facilitated by the tendency of porous materials to create velocity oscillations that alter the Reynolds stress profile along the material thickness. Concurrently, this creates a more rapid recovery of the momentum deficit in the wake, determined by the positive 'flow communication' between the boundary layer and the wake regions (as also seen in previous studies by Koh *et al*. (2018) and Showkat Ali *et al*. (2020)). In particular, the flow communication entails a non-negligible velocity correlation in fluid regions separated by the object.

3.2. Unsteady-flow features

In this section, attention is drawn to three regions: the boundary layer, the shear layer generated at the trailing edge and the deeper wake flow. Spectra of the vorticity and pressure signals are computed from the super-sampled time-resolved flow field at the three aforementioned locations corresponding to P1(–0.20, 0.60), P2(1, 0.5), P3(2, 0), and depicted by red marks in figure 5. The left column of figure 5 presents maps of instantaneous non-dimensionalised vorticity magnitude for the (a) STE, (d) SPTE and (g) RFTE, to assist the visualisation of the flow field at the three selected points. Panels in the middle and right columns of figure 5 are auto-spectra of vorticity and pressure fluctuations calculated at the three locations. The spectra of both vorticity and pressure fluctuations at P1 show a relatively broadband distribution, consistent with the turbulent frequency distribution of a fully developed boundary layer. The distribution of the SPTE presents a lower-frequency content (i.e. $St < 1$) with respect to both STE and RFTE, possibly due to the interaction of flow scales at the pore level with the SPTE geometry (Arcondoulis *et al*. 2025). For all configurations, the maximum energy content remains centred in the

https://doi.org/10.1017/flo.2026.10053 Published online by Cambridge University Press

range St = [0.2–1], with no relevant peak observed at the shedding frequency St = 0.2 at the P1 locations. Since the characteristics of the incoming boundary layer are very similar across the three cases, the auto-spectral distributions of both vorticity and pressure are similarly broadband before separating at the edge. Further downstream at P2, both the permeable and solid trailing edges exhibit a narrowband contribution centred on the shedding frequency in the vorticity and pressure auto-spectra. More precisely, the spectral contribution from the vortex shedding can be seen to be building up already at x/t = 1; at a Strouhal number of 0.2 based on the thickness t, corresponding to approximately f = 1.2 Hz, the pressure spectra of both configurations exhibit a peak. Both permeable materials mitigate vortex shedding, as evidenced by the lower peak values at St = 0.2, consistent with the literature (Geyer 2020). A secondary peak at St = 1 (f = 6 Hz) is observed for the SPTE, which is not visible for the RFTE, originating from the element size of the structured porous insert. The spectra at P3 reveal a relatively broadband distribution for both SPTE and RFTE, while the STE still shows peaks at St = 0.2 and its harmonic St = 0.4, due to the scalar nature of the pressure fluctuations, which do not distinguish between co- and counter-rotating vorticity. It is also important to comment on the high-frequency harmonics in the pressure spectra. This series of harmonics, at a multiple of 10 Hz (St = 1.7), corresponds to the acquisition frequency of the cameras from which the super-sampled time series is created. Since the super-sampling process propagates the vector fields back and forth from the instantaneous series at a low repetition rate, a change in the masked series of vectors determines a small change in the boundary conditions of the pressure fluctuation, recorded as noise at that specific frequency.

4. Flow communication through permeable materials

Before deriving the dynamic permeability function, this section demonstrates how flow propagates through the material. We first quantify this flow communication using velocity correlations. Proper orthogonal decomposition (POD) is then employed to further isolate and visualise the dominant regions where this communication occurs. By separating coherent flow structures, POD highlights how different materials influence the spatial distribution of flow penetration. Accordingly, the first part of the section presents the velocity-correlation analysis, while the second part shows how regions of strong POD-identified flow communication provide insight into the material's dynamic permeability response.

4.1. Spectral analysis of velocity and vorticity

Maps of instantaneous vorticity together with the spectral analysis of the vorticity and the magnitude-squared coherence of the vertical-velocity fluctuations (i.e. magnitude of $C_{v,v}$) and the wall-normal velocity fluctuations (i.e. magnitude of $C_{v,u}$) are presented in figure 6. The results for the STE are presented in the top row, the SPTE results in the middle row and the RFTE results in the bottom row. The spectral analysis of the vortical fluctuations is performed by plotting the power spectral density at different locations within the middle column. While the point in the boundary layer is kept the same as before, now indicated by P4(−0.20, 0.60), new points are chosen and analysed in the direct proximity of the sample wall: P5(0.05, 0.40), P6(0.05, 0.35), P7(0.05, 0.30), P8(0.05, 0.25). The point distribution is chosen to highlight the energy content of fluctuations near the sample trailing edges compared with those in the boundary layer. Starting from the STE, the energy content of the vortical fluctuations in the wake of the object (points P5–P8) is negligible with respect to the vorticity content in the boundary layer (point P4), as can be seen in figure 6b. The magnitude-squared coherence in figure 6c shows very low correlation between the vertical flow fluctuations in the boundary layer and those just behind the sample thickness for both vertical and normal components. This is consistent with the fact that, since the STE is non-permeable, the flow velocity in the separated region at the trailing edge approaches zero. Therefore, velocity fluctuations in the boundary layer are mostly shielded by the separated region and convected downstream. Comparing the results with figure 6e, the SPTE shows relatively higher content of the flow fluctuations at the same locations in the wake, mostly below $St \approx 2$. The magnitude-squared coherence

https://doi.org/10.1017/flo.2026.10053 Published online by Cambridge University Press

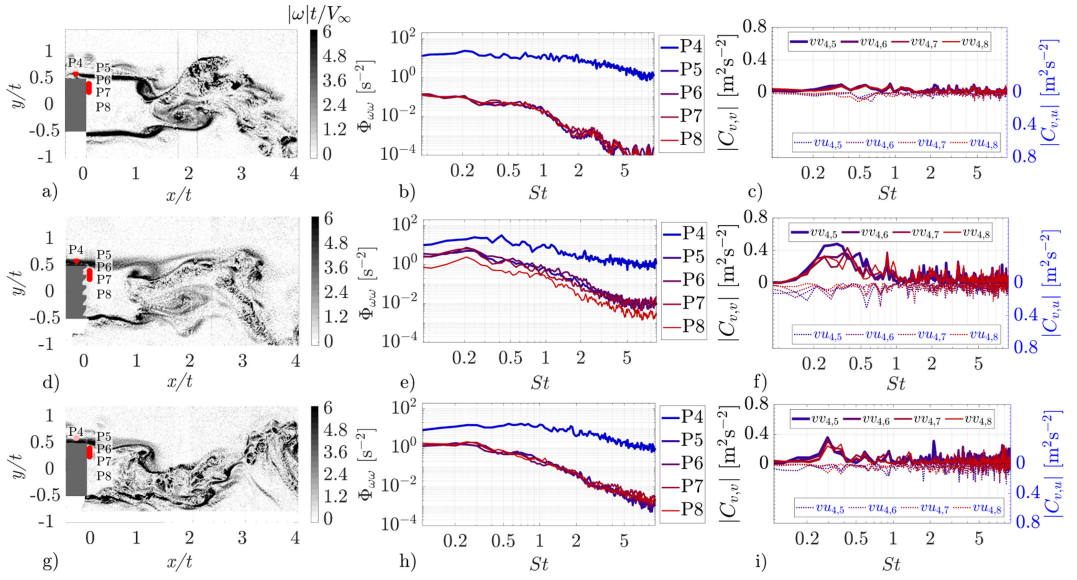


Figure 6. *Maps of vorticity magnitude in the left column superimposed to the locations of the one point in the boundary layer P4, and four points in the wake, P5–P8, at which the spectral density (middle column) of vorticity and the magnitude-squared coherence (right column) of both the vertical and wall-normal velocity components as extracted from the points are computed for (a–c) the STE, (d–f) the SPTE and (g–i) the RFTE. We note that P4 corresponds to P1 in figure 5. Additionally, the wall-normal components are plotted mirrored with a second axis on the right of the graph, pointing downward.*

in figure 6f also shows stronger similarity of the vertical flow fluctuations in a range below $St \approx 1$ with respect to the fluctuations in the boundary layer. Relatively lower is the similarity of the wall-normal components for the two locations, which are still non-negligible in the same frequency range of the vertical flow fluctuations. Relatively higher fluctuations of vorticity with respect to the STE are additionally measured for the RFTE in figure 6h, although of lower value than those of the SPTE, possibly due to the smaller uniform pore size in all directions within the material. This dampening effect of fluctuations with relatively lower frequencies is also confirmed by the magnitude-squared coherence of both vertical and wall-normal components in figure 6i, which resembles that of the STE, albeit with slightly higher similarity in the low-frequency range. The presence of vortical flow structures with velocity fluctuations similar to those in the boundary layer for permeable materials can be taken as indirect evidence of flow communication, which is predominantly observed at $St < 1$ for both permeable materials. The differences in the magnitude-squared coherence between the SPTE and RFTE can be attributed to the distinct structures of the two materials, with the SPTE promoting communication at frequencies proportional to its pore size. By additionally investigating the spectral content across points from P5 to P8 for SPTE and RFTE, it can be observed that, while the RFTE shows a nearly identical distribution across points, the SPTE spectral content decreases with increasing distance from the boundary layer. This is an effect of the channel distribution in the SPTE: the farther from the boundary layer, the greater the pressure losses imposed on the flow, which dissipate the vortical fluctuations along the paths. An aspect common to the two porous materials is that flow fluctuations with higher-frequency responses corresponding to flow structures smaller than half the pore size do not obviously correlate with each other over the measured distance, since they are dissipated before. This means that for $St > 2$, no correlation can be effectively measured.

https://doi.org/10.1017/flo.2026.10053 Published online by Cambridge University Press

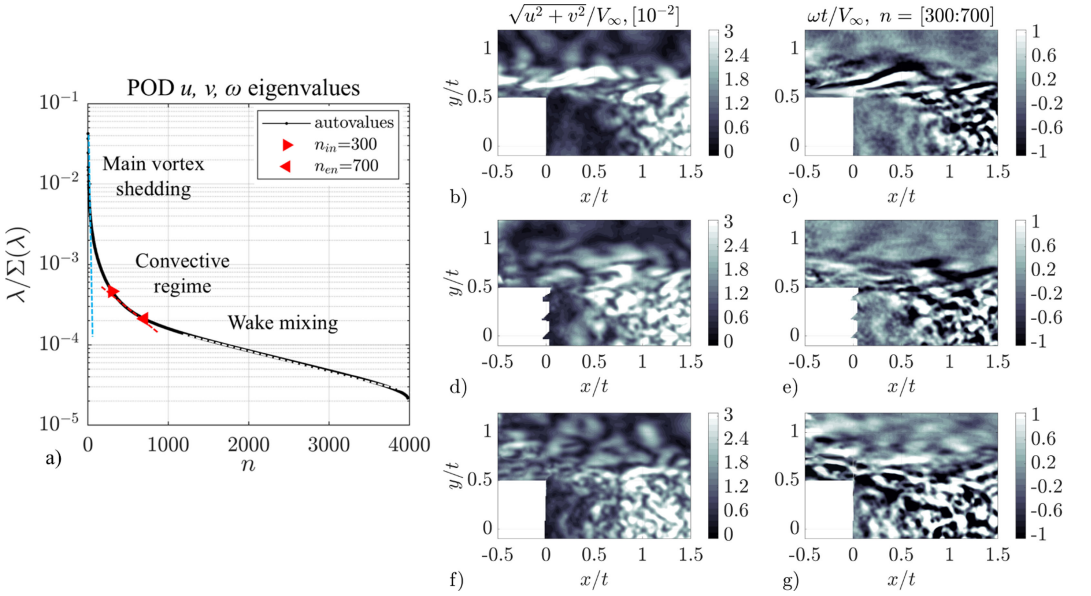


Figure 7. *Low-order reconstruction of one super-sampled time series based upon POD based on its singular value decomposition, in the range $n = 300 < n < 700$ as shown in (a) for the STE (b, c), SPTE (d, e) and RFTE (f, g). The fluctuations of velocity are reconstructed for one of the frames in fields b–d–f, and the vorticity ones in c–e–g. The modal energy distribution in (a) is presented only for the STE, since the SPTE and RFTE ones are very similar.*

4.2. Proper orthogonal decomposition

Despite yielding key insights into the flow communication process, the spectra presented in figures 5 and 6 do not provide quantitative indications of the spatio-temporal convection of the flow structures involved in the process and their organisation. Further clarification of these aspects can be obtained by visualising the velocity fluctuations in the boundary layer and the near-field region of the wake. To retain exclusively the velocity fluctuations expected within the flow communication, a filtering procedure based on POD is applied (Berkooz *et al*. 1993; Lumley 1967). The distribution of the normalised eigenvalues pertaining to the POD mode decomposition of the velocity fields for all materials is computed. The eigenvalue distribution in figure 7a for the STE is shown for reference, since the ones for RFTE and SPTE follow a very similar trend. It is verified that the modes with the eigenvalue distribution in figure 7a can be divided into three ranges. The first range of high-energy modes corresponds to flow structures of the same size as the vortex shedding, and their energy decays logarithmically with increasing POD modes (blue dashed line). The intermediate range corresponds to the convective regime of the high-frequency structures, marking a change in slope in the graph (red dashed line). The last region with relatively low-energy content contains flow structures from wake mixing and the residual of the decomposition (black dashed line). A low-order reconstruction from the POD mode decomposition is computed in the region of the change of slope. The higher-energy modes are intentionally neglected to isolate the high-frequency distribution of flow structures that can be convected through the permeable materials in the vicinity of the recirculation region. The reconstructed velocity and vorticity fields are presented in figure 7. In particular, the reconstructed velocity and vorticity fields are presented for the STE in figures 7b and 7c, for the SPTE in figures 7d and 7e and for the RFTE in figures 7f and 7g.

In figures 7b and 7c, the low-order reconstruction is shown for the STE. By observing the velocity components and vorticity fluctuations, a stagnation region can be identified behind the STE. The fluctuations with high spatial frequency from the boundary layer are convected directly downstream to

https://doi.org/10.1017/flo.2026.10053 Published online by Cambridge University Press

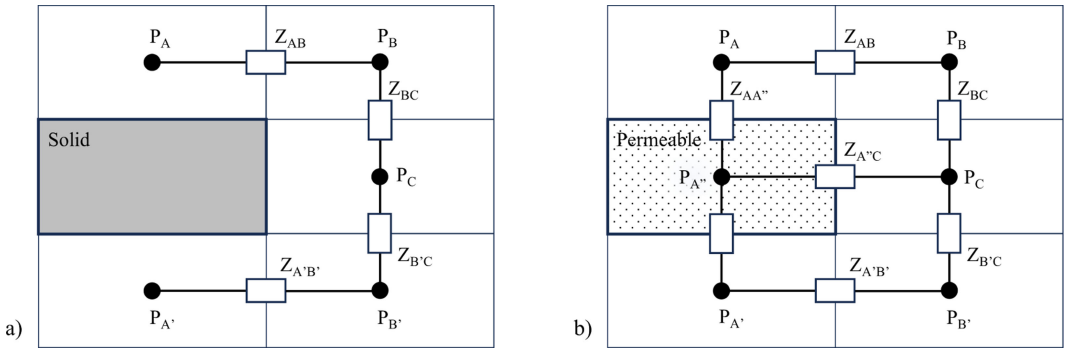


Figure 8. *Conceptual schematic diagram of (a) the lumped-system model for the STE (for reference), and (b) lumped-system model for the permeable trailing edge. The Z-terms represent flow impedances connecting pressure points at different locations.*

$x/t \approx 1$. Due to the non-permeability of the trailing edge, very low amplitude residuals of large fluctuations can be measured in the recirculation region. Figures 7d and 7e present the same distribution for the SPTE. A clear difference in mixing is observed with vortical flow structures seeping through the porosity. The low-order reconstruction also shows high-spatial-frequency fluctuations, proportional to the cell-unit size, permeating the material. Due to the pore dimensions, fluctuations with spatial dimensions below the millimetre level are more prominent. These correspond to a Strouhal number of approximately 1, assuming a convective velocity through the material approximately one tenth that of the boundary layer. In figures 7f and 7g, the comparison is extended to the trailing edge of the randomised foam. The uniform, equally distributed pore size in the randomised foam results in a clear increase in the high-frequency fluctuations in the wake region. Fluctuations with a spatial dimension larger than the pore size are statistically uniformly distributed in the wake region due to the pore size of the randomised foam, supporting the previous conclusions from figure 6.

4.3. Transfer function evaluation from the unsteady-flow data

In this section, a lumped-model approach is proposed to evaluate the dynamic response of permeability in porous materials subjected to grazing flows. The approach enables direct assessment of the material's unsteady response from flow information, thereby extending conventional approaches. The time-averaged parameters are typically obtained by curve fitting the experimental pressure drop in a channel with a uniform section, based on the Hazen–Dupuit–Darcy equation (Geyer 2020; Narasimhan 2013; Rubio-Carpio *et al*. 2019). The approach of this study relates the unsteady response of velocity fluctuations to the unsteady pressure gradient, comparing the results with the theoretical model proposed by Johnson *et al*. (1987). To describe the lumped-system approach, a schematic is presented in figure 8a is proposed. The problem is simplified by considering only the neighbouring pressure at the points P_A and P_C. Clearly, points farther from the object are not considered in the system, as they can be assimilated to an equivalent impedance in the AB direction, providing a contribution that is already accounted for in the circuit. When considering one side of the circuit, the points P_A and P_C are either connected through a fluid impedance when considering the solid STE case in figure 8a, or both through fluid and material paths. The circuit analogy stands behind the fact that, if we consider the permeable material, an incompressible stream tube (i.e. density, ρ, is constant) with momentum flux $\rho A_A V_A$ is split in P_A into two components, a contribution $\rho A_m v_m$ through the material path AA", and a remaining one $\rho A_f v_f$ through the fluid path AB. The terms v_m and v_f are respectively the velocity at the material interface and convected along AB, while A_n and A_f are respectively the interfacial area through the material and the one perpendicular to the fluid path. The same pressure differential is established between the same nodal points. To describe the material properties, the current study refers to the formulations of

https://doi.org/10.1017/flo.2026.10053 Published online by Cambridge University Press

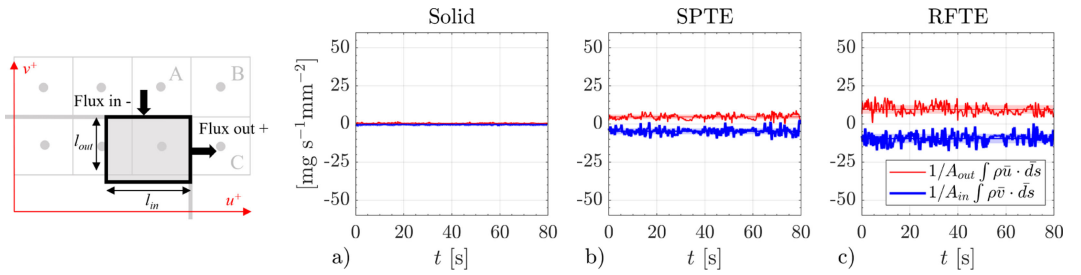


Figure 9. *Orientation of fluxes and their evaluation for the (a) STE, (b) SPTE and (c) RFTE. Note that the two super-sampled series are added one after the other in the plot.*

Cortis *et al*. (2003) and Johnson *et al*. (1987), which were obtained by averaging the material properties over disturbances with wavelengths larger than the channel's pore size. Additionally, for this specific application, we demonstrate that there is negligible communication along the path AA"A' due to the material's thickness with respect to the incoming boundary layer. The differential equations along the circuits are

$$\begin{cases} ABC: & \nabla p = \left[-\rho\left(\dfrac{dv_f}{dt} + v_f\dfrac{dv_f}{ds}\right) + \mu\dfrac{d^2v_f}{ds^2}\right], \\ AA''C: & \nabla p = -\mu\dfrac{\phi}{k(\omega)}v_m, \end{cases} \tag{4.1}$$

where ∇p is the gradient of pressure through the indicated paths, ϕ is the open area or porosity, K is the dynamic permeability and s is the path coordinate. For simplicity, all velocity contributions along the paths are averaged over their length. Of primary interest is the ratio of the pressure difference across the two points along the AC path to the velocity through the material, which determines the dynamic permeability experimentally. Here, the relationship between the exiting velocity and the measurement of unsteady pressure fluctuations at two different nodes of the material is targeted. As discussed by Cortis *et al*. (2003), by considering only the fluctuating part of the signal in the velocity and pressure gradient in (4.1), it is possible to frame an electrical analogy where the pressure differential is analogous to an equivalent circuit voltage. In this analogy, if the elements ρv_f and ρv_m are assumed to be circuit currents, then the material branch of the circuit contributes with an equivalent resistance, while the fluid branch includes more complex equivalent impedance, which can be reformulated as equivalent inductance and capacitance.

To validate the approach, it is important to make sure that the fluxes through the material are consistent with the model presented above. For this analysis, it is possible to monitor, for a given pressure difference between the two nodes, the spatial distribution of the fluid velocity, which, when fed to (4.1), yields an approximation of the dynamic permeability, k. In figure 9, the fluxes through the material are first plotted versus time in the corner region according to the convention shown above. In particular, due to the thickness t of the porous sample, a $t/2$ length is used to compute the vertical fluxes, with the horizontal length adjusted to maintain the same mass flow. It is verified that in the present study, comparable lengths along the horizontal direction balance the fluxes in the vertical direction. For materials with highly inhomogeneous porosity across different boundaries, the two lengths should be proportionally adjusted, since the assumption of mass flow conservation must be verified. Additionally, in the present study, the actual values of the normalised fluxes per unit area already converge from a $t/6$ length, which is consistent with the pore dimension size of the adopted materials. Those correspond to the flux that enters the material from element B in figure 9 and the outward flux exiting from the material, i.e. the outward element E in the same figure. The left figure pertains to the solid configuration, the middle figure to the SPTE, and the right to the RFTE. The plots confirm the presence of a non-negligible amount of incoming and outgoing flow for the permeable materials. The average entering and exiting mass fluxes at the top and lateral sides are found to have opposite signs, confirming that the flow enters from the boundary-layer sides and exits from the side exposed to the wake.

https://doi.org/10.1017/flo.2026.10053 Published online by Cambridge University Press

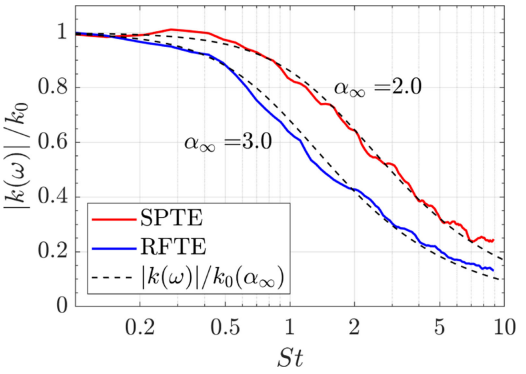


Figure 10. *Dynamic permeability derived from the unsteady fluctuations using (4.1). The coloured lines are derived from time-resolved PIV, while the black lines are obtained from Johnson et al. (1987). Fitted values for the SPTE and RFTE are respectively:* Λ *= [0.5, 0.8] mm. Dashed curves are derived for* α_∞ *= [2, 3].*

The velocity, v_m, is computed at the direct exit of the permeable material, since the fluxes exiting the material exhibit a lower uncertainty than the incoming ones. In figure 10, the value of the normalised frequency-dependent response of permeability is computed by using the experimental data and compared with the theoretically expected behaviour from Johnson *et al*. (1987). The analytical model is depicted in figure 10 in black and was derived using the uniform and homogeneous parameters in table 2. The experimental counterpart of the dynamic permeability is derived by averaging the velocity and the pressure difference over the previously indicated $t/2$ horizontal and vertical lengths. The pressure gradient is computed as the instantaneous difference of the spatially averaged pressure between the two horizontal and vertical sides of the corners. We remind the reader that the experimental values are obtained by using the second row of (4.1), once again normalised by the known parameters of table 2. Therefore, two different decays are derived for the two materials. The model also allows for extracting the equivalent tortuosity and the viscous length-scale values by overlapping the experimental response with the analytical one. Both measured curves compare with a very similar decay in frequency to the analytical formula from Johnson *et al*. (1987), using the estimated parameters above. A slightly higher response is observed experimentally for the SPTE than for the RFTE; however, the values are very close. In particular, from the study of Johnson *et al*. (1987), a tortuosity of between 2 and 4 should correspond to an arbitrary homogeneous and isotropic distribution of channels proportional to the pore size length. The extracted parameters are $\Lambda = [0.5, 0.8]$ mm and $\alpha_\infty = [2, 3]$ respectively for the SPTE and for the RFTE. This is consistent with the derivation from Johnson *et al*. (1987) showing that the viscous length scales should correspond to a fraction of the pore size. By combining the flow results with the dynamic-permeability analysis, we observe that the SPTE behaves with a higher permeability response than the RFTE at high frequency. These trends reflect the influence of the material's internal architecture, which appears to restrict flow communication somewhat more than the RFTE at higher Strouhal numbers. Although the differences between the two materials are small, they are still meaningful: they help explain why the acoustic performances of the SPTE and RFTE are reported to be comparable (Arcondoulis *et al*. 2024, 2025), despite the SPTE exhibiting somewhat better aerodynamic drag performance and the RFTE showing a slightly faster wake recovery in the flow measurements.

5. Conclusions

A new experimental method is developed and demonstrated for measuring the dynamic permeability of porous trailing edges under grazing flow, based on time-resolved PIV and a lumped-system circuit analogy. Unlike conventional steady-flow rig measurements, this approach operates directly in the aerodynamic environment of interest and accommodates thin trailing-edge geometries. An experimental

https://doi.org/10.1017/flo.2026.10053 Published online by Cambridge University Press

study using time-resolved PIV in water was conducted to investigate how materials with similar porous characteristics elicit different unsteady-flow responses. Depending on the internal flow path, locally correlated flow velocity fluctuations indicate that the scales of velocity fluctuations depend on the material's inner parameters, which indirectly affect different flow frequencies with different response amplitudes. Mean results and fluctuations indicate that the integral effect of the flow communication determines a different outcome in the turbulent wake of the various materials. The spectra of both vorticity and pressure fluctuations transition from broadband to narrow-band, with communication across a range of Strouhal frequencies from approximately 0.2 to approximately 1. A method to quantify the effective response function of the material to velocity fluctuations is proposed, based on circuit analysis, which assumes a lumped system comprising different elements within the material. The approach enables the measurement and validation of the material's dynamic-permeability response under grazing conditions and allows comparison with existing analytical response functions. At relatively higher Strouhal number, the measured permeability curves exhibit differences in decay slope between the SPTE and RFTE. These differences are consistent with the expectation that microstructural features, such as pore orientation and flow-path tortuosity, can influence the frequency response. While the present data do not isolate the specific mechanisms responsible, the observed trend suggests that internal architecture may play a role in shaping the high-frequency decay, warranting further targeted investigation. This methodology can be extended beyond trailing-edge noise control to a wide range of permeable bluff-body and porous-wall problems in fluid mechanics, such as ventilation in bio-inspired surfaces, flow control in turbomachinery or the characterisation of permeable sediment beds in environmental flows. Enabling *in situ* measurement of dynamic permeability under realistic operating conditions opens a pathway to rapidly linking material design parameters with their aerodynamic and acoustic performance.

Supplementary material. The supplementary material for this article can be found at https://doi.org/10.1017/flo.2026.10053.

Data availability statement. Raw data are available from the corresponding author.

Author contributions. D. R., D. F. and E. J. G. A. created the research plan, designed and performed the experiments. D. R. additionally wrote the manuscript, which has been reviewed multiple times by D. F. and E. J. G. A.

Funding statement. The authors acknowledge the Dutch Research Council (NWO) for financing the study under the Open Technology Program: Aeroacoustic Multi-path Permeable geometries for airfoil Edge noise REduction, AMPERE, TTW-OTP grant number 20467.

Competing interests. The authors declare no conflicts of interest.

Ethical standards. The research adheres to all ethical guidelines, including compliance with the legal requirements of the study country.

References

Achenbach, E. (1971). Influence of surface roughness on the cross-flow around a circular cylinder. *Journal of Fluid Mechanics*, *46*(2), 321–335.

Adrian, R. J., & Yao, C. S. (1985). Pulsed laser technique application to liquid and gaseous flows and the scattering power of seed materials. *Applied Optics*, *24*(1), 44–52.

Ali, S. A. S., Azarpeyvand, M., & Da Silva, C. R. I. (2018). Trailing-edge flow and noise control using porous treatments. *Journal of Fluid Mechanics*, *850*, 83–119.

Arcondoulis, E. J. G., Liu, Y., Li, Z., Yang, Y., & Wang, Y. (2019). Structured porous material design for passive flow and noise control of cylinders in uniform flow. *MDPI-Materials*, *12*(18), 2905.

Arcondoulis, E. J. G., Liu, Y., Ragni, D., Avallone, F., Rubio-Carpio, A., Sedaghatizadeh, N., Yang, Y., & Li, Z. (2023). Internal shear layer and vortex shedding development of a structured porous coated cylinder using tomographic particle image velocimetry. *Journal of Fluid Mechanics*, *967*, A17.

Arcondoulis, E. J. G., Ragni, D., Fiscaletti, D., & Merino-Martinez, R. (2025). Near-wall and wake flow fields of a blunt trailing edge appended with structured and randomised porous media. *Flinovia – Flow Induced Noise and Vibration Issues and Aspects, Conference Paper*, *4*, 305–330.

https://doi.org/10.1017/flo.2026.10053 Published online by Cambridge University Press

Arcondoulis, E. J. G., Ragni, D., Fiscaletti, D., Merino-Martinez, R., & Liu, Y. (2024). Acoustic response of structured and randomized porous blunt trailing edges subject to turbulent boundary layers. *The Journal of the Acoustical Society of America*, *156*(2), 1029–1040.

Barbi, C., Favier, D. P., Maresca, C. A., & Telionis, D. P. (1986). Vortex shedding and lock-on of a circular cylinder in oscillatory flow. *Journal of Fluid Mechanics*, *170*, 527–544.

Bearman, P. W. (1965). Investigation of the flow behind a two-dimensional model with a blunt trailing edge and fitted with splitter plates. *Journal of Fluid Mechanics*, *21*(2), 241–255.

Berkooz, G., Holmes, P., & Lumley, J. L. (1993). The proper-orthogonal decomposition in the analysis of turbulent flows. *Annual Review of Fluid Mechanics*, *25*, 539–575.

Blake, W. K. (2012). *Mechanics of flow-induced sound and vibration* (*V1-2*). Elsevier.

Boillot, A., & Prasad, A. K. (1996). Optimization procedure for pulse separation in cross-correlation piv. *Experiments in Fluids*, *21*(2), 87–93.

Brooks, T. F., Pope, D. S., & Marcolini, M. A. (1989). Airfoil self-noise and prediction. Report Number: NASA-RP-1218, NASA Reference Publication.

Chandler, R. N. (1981). Transient streaming potential measurements on fluid-saturated porous structures: An experimental verification of biot's slow wave in the quasi-static limit. *The Journal of the Acoustical Society of America*, *70*(1), 116–121.

Charlaix, E., Kushnick, A., & Stokes, J. (1988). Experimental study of dynamic permeability in porous media. *Physical Review Letters*, *61*(14), 1595.

Charonko, J. J., King, C. V., Smith, B. L., & Vlachos, P. P. (2010). Assessment of pressure field calculations from particle image velocimetry measurements. *Measurement Science and Technology*, *21*(10), 105401.

Cortis, A., Smeulders, D. M. J., Guermond, J. L., & Lafarge, D. (2003). Influence of pore roughness on high-frequency permeability. *Physics of Fluids*, *45*(6), 1766–1775.

de Kat, R., & van Oudheusden, B. W. (2012). Instantaneous planar pressure determination from piv in turbulent flow. *Experiments in Fluids*, *52*, 1089–1106.

Geyer, T. F. (2020). Experimental evaluation of cylinder vortex shedding noise reduction using porous material. *Experiments in Fluids*, *61*, 1–21.

Geyer, T. F., Sarradj, E., & Fritzsche, C. (2010a). Measurement of the noise generation at the trailing edge of porous airfoils. *Experiments in Fluids*, *48*, 291–308.

Geyer, T. F., Sarradj, E., & Fritzsche, C. (2010b). Porous airfoils: Noise reduction and boundary layer effects. *International Journal of Aeroacoustics*, *9*(6), 787–820.

Ghaemi, S., Ragni, D., & Scarano, F. (2012). Piv-based pressure fluctuations in the turbulent boundary layer. *Experiments in Fluids*, *53*(6), 1823–1840.

Graham, R. R. (1934). The silent flight of owls. *The Aeronautical Journal*, *38*(286), 837–843.

Jaworski, J. W., & Peake, N. (2020). Aeroacoustics of silent owl flight. *Annual Review of Fluid Mechanics*, *52*(1), 395–420.

Johnson, D. L., Koplik, J., & Dashen, R. (1987). Theory of dynamic permeability and tortuosity in fluid-saturated porous media. *Journal of Fluid Mechanics*, *176*, 379–402.

Kiu, K. Y., Stappenbelt, B., & Thiagarajan, K. P. (2011). Effects of uniform surface roughness on vortex-induced vibration of towed vertical cylinders. *Journal of Sound and Vibration*, *330*(20), 4753–4763.

Klausmann, K., & Ruck, B. (2017). Drag reduction of circular cylinders by porous coating on the leeward side. *Journal of Fluid Mechanics*, *813*, 382–411.

Koh, S. R., Meinke, M., & Schröder, W. (2018). Numerical analysis of the impact of permeability on trailing-edge noise. *Journal of Sound and Vibration*, *421*, 348–376.

Kwon, K., & Choi, H. (1996). Control of laminar vortex shedding behind a circular cylinder using splitter plates. *Physics of Fluids*, *8*(2), 479–486.

Lafarge, D., Lemarinier, P., Allard, J. F., & Tarnow, V. (1997). Dynamic compressibility of air in porous structures at audible frequencies. *The Journal of the Acoustical Society of America*, *102*(4), 1195–2006.

Lasseux, D., Valdés-Parada, F. J., & Bellet, F. (2019). Macroscopic model for unsteady flow in porous media. *Journal of Fluid Mechanics*, *862*, 283–311.

Lee, T., & Budwig, R. (1991). The onset and development of circular-cylinder vortex wakes in uniformly accelerating flows. *Journal of Fluid Mechanics*, *232*, 611–627.

Liu, H., Hu, Z., Chen, N., Liu, Y., & Fan, H. (2023). Structured porous blunt trailing edge with uniform and non-uniform parameters for vortex shedding noise reduction. *Applied Acoustics*, *206*, 109302.

Lumley, J. L. (1967). The structure of inhomogeneous turbulent flows. *Atmospheric Turbulence and Radio Wave Propagation*, *7*, 166–178.

Maryami, R., Arcondoulis, E. J. G., Liu, Q., & Liu, Y. (2023). Experimental near-field analysis for flow induced noise of a structured porous-coated cylinder. *Journal of Sound and Vibration*, *551*, 117611.

McClure, J., & Yarusevych, S. (2017). Optimization of planar PIV-based pressure estimates in laminar and turbulent wakes. *Exp Fluids 58*, 62. https://doi.org/10.1007/s00348-017-2337-7

Naito, H., & Fukagata, K. (2012). Numerical simulation of flow around a circular cylinder having porous surface. *Physics of Fluids*, *24*(11), 117102.

https://doi.org/10.1017/flo.2026.10053 Published online by Cambridge University Press

Nakamura, Y. (1996). Vortex shedding from bluff bodies and a universal strouhal number. *Journal of Fluids and Structures*, *10*(2), 159–171.

Narasimhan, A. (2013). *Essentials of heat and fluid flow in porous media* (Vol. 61). CRC Press, Taylor & Francis, Group.

Okajima, A. (1982). Strouhal numbers of rectangular cylinders. *Journal of Fluid Mechanics*, *123*, 379–398.

Pröbsting, S., Scarano, F., Bernardini, M., & Pirozzoli, S. (2013). On the estimation of wall pressure coherence using time-resolved tomographic piv. *Experiments in Fluids*, *54*(7), 1–15.

Raffel, M., Willert, C., Scarano, F., Kähler, C., Wereley, S., & Kompenhans, J. (2018). *Particle image velocimetry - a practical guide*. Springer.

Ragni, D., Ashok, A., van Oudheusden, B. W., & Scarano, F. (2009). Surface pressure and aerodynamic loads determination of a transonic airfoil based on particle image velocimetry. *Measurement Science and Technology*, *20*(7), 074005.

Ragni, D., Avallone, F., van der Velden, W. C. P., & Casalino, D. (2019). Measurements of near-wall pressure fluctuations for trailing-edge serrations and slits. *Experiments in Fluids*, *60*(6), 1–22.

Roshko, A. (1954). NATIONAL ADVISORY COMMITTEE F FOR AERONAUTICS.4 TECHNICAL NOTE 2913 ON THE DEVELOPMENT OF TURBULENT WAKES FROM VORTEX STREETS 1, By Anatol Roshko California Institute of Technology.

Rubio-Carpio, A., Merino-Martínez, R., Avallone, F., Ragni, D., Sneller, M., & van der Zwaag, S. (2019). Experimental characterization of the turbulent boundary layer over a porous trailing edge for noise abatement. *Journal of Sound and Vibration*, *443*, 537–558.

Scarano, F., & Moore, P. (2012). An advection-based model to increase the temporal resolution of piv time series. *Experiments in Fluids*, *52*, 919–933.

Scarano, F., & Riethmuller, M. L. (1999). Iterative multigrid approach in PIV image processing with discrete window offset. *Experiments in Fluids*, *26*(6), 513–523.

Schrijer, F. F. J., & Scarano, F. (2008). Effect of predictor–corrector filtering on the stability and spatial resolution of iterative piv interrogation. *Experiments in Fluids*, *45*(5), 927–941.

Sheng, P., & Zhou, M. Y. (1988). Dynamic permeability in porous media. *Physical Review Letters*, *61*(14), 1591–1594.

Showkat Ali, S. A., Azarpeyvand, M., & Ilário da Silva, C. R. (2020). Trailing edge bluntness noise reduction using porous treatments. *Journal of Sound and Vibration*, *474*, 115257.

Sueki, T., Takaishi, T., Ikeda, M., & Arai, N. (2010). Application of porous material to reduce aerodynamic sound from bluff bodies. *Fluid Dynamics Research*, *42*(1), 015004.

Teruna, C., Avallone, F., Ragni, D., Rubio-Carpio, A., & Casalino, D. (2021). Numerical analysis of a 3-D printed porous trailing edge for broadband noise reduction. *Journal of Fluid Mechanics*. *926*:A17. https://10.1017/jfm.2021.704.

van Oudheusden, B. W. (2013). Piv-based pressure measurement. *Measurement Science and Technology*, *24*(3), 032001.

Violato, D., Moore, P., & Scarano, F. (2011). Lagrangian and eulerian pressure field evaluation of rod-airfoil flow from time-resolved tomographic piv. *Experiments in Fluids*, *50*, 1057–1070.

Wood, B. D., He, X., & Apte, S. V. (2020). Modeling turbulent flows in porous media. *Annual Review of Fluid Mechanics*, *52*, 171–203.

Cite this article: Ragni D., Arcondoulis E. J. G. and Fiscaletti D. (2026). Measurement of dynamic permeability in grazing flows for porous trailing edges. *Flow*, *6*, E16. https://doi.org/10.1017/flo.2026.10053

https://doi.org/10.1017/flo.2026.10053 Published online by Cambridge University Press